

## James Spencer Lundh

Department of Mechanical Engineering,  
The Pennsylvania State University,  
University Park, PA 16802

## Yiwen Song

Department of Mechanical Engineering,  
The Pennsylvania State University,  
University Park, PA 16802

## Bikramjit Chatterjee

Department of Mechanical Engineering,  
The Pennsylvania State University,  
University Park, PA 16802

## Albert G. Baca

Sandia National Laboratories,  
Albuquerque, NM 87185

## Robert J. Kaplar

Sandia National Laboratories,  
Albuquerque, NM 87185

## Andrew M. Armstrong

Sandia National Laboratories,  
Albuquerque, NM 87185

## Andrew A. Allerman

Sandia National Laboratories,  
Albuquerque, NM 87185

## Brianna A. Klein

Sandia National Laboratories,  
Albuquerque, NM 87185

## Dustin Kendig

Microsanj, LLC,  
Santa Clara, CA 95051

## Hyungtak Kim

School of Electronic and Electrical Engineering,  
Hongik University,  
94, Wausan-road, Mapo-gu,  
Seoul 04066, South Korea

## Sukwon Choi<sup>1</sup>

Department of Mechanical Engineering,  
The Pennsylvania State University,  
University Park, PA 16802

# Device-Level Multidimensional Thermal Dynamics With Implications for Current and Future Wide Bandgap Electronics

*Researchers have been extensively studying wide-bandgap (WBG) semiconductor materials such as gallium nitride (GaN) with an aim to accomplish an improvement in size, weight, and power of power electronics beyond current devices based on silicon (Si). However, the increased operating power densities and reduced areal footprints of WBG device technologies result in significant levels of self-heating that can ultimately restrict device operation through performance degradation, reliability issues, and failure. Typically, self-heating in WBG devices is studied using a single measurement technique while operating the device under steady-state direct current measurement conditions. However, for switching applications, this steady-state thermal characterization may lose significance since the high power dissipation occurs during fast transient switching events. Therefore, it can be useful to probe the WBG devices under transient measurement conditions in order to better understand the thermal dynamics of these systems in practical applications. In this work, the transient thermal dynamics of an AlGaIn/GaN high electron mobility transistor (HEMT) were studied using thermoreflectance thermal imaging and Raman thermometry. Also, the proper use of iterative pulsed measurement schemes such as thermoreflectance thermal imaging to determine the steady-state operating temperature of devices is discussed. These studies are followed with subsequent transient thermal characterization to accurately probe the self-heating from steady-state down to submicrosecond pulse conditions using both thermoreflectance thermal imaging and Raman thermometry with temporal resolutions down to 15 ns. [DOI: 10.1115/1.4047100]*

**Keywords:** gallium nitride (GaN), high electron mobility transistor (HEMT), power electronics, Raman thermometry, self-heating, thermal dynamics, thermal management, thermoreflectance thermal imaging, wide bandgap (WBG)

## 1 Introduction

Wide bandgap semiconductor materials such as silicon carbide (SiC) and gallium nitride (GaN) have been replacing silicon (Si) as the standard material in high frequency and high power

electronics [1–7]. While SiC has high thermal conductivity [8] suggesting superior thermal performance, GaN has reasonably high thermal conductivity [8] in addition to numerous superior electronic properties. These include its wide bandgap ( $E_G \sim 3.4$  eV), high breakdown field, and high saturation velocity [8–11]. These material properties are promising for high temperature, high voltage, and high frequency operation. Furthermore, due to spontaneous and piezoelectric polarization effects in AlGaIn/GaN heterostructures [12,13], high electron mobility transistor (HEMT) structures can be fabricated that utilize a two-dimensional electron gas (2DEG) as the device current channel. The high carrier concentration and mobility in the 2DEG result in reduced sheet resistance, lowering conduction losses [14–16]. The high breakdown field also allows fabrication of shorter channel devices; in combination with the high saturation velocity and high mobility, this can lead to reduced switching losses [14–16].

<sup>1</sup>Corresponding author.

Contributed by the Electronic and Photonic Packaging Division of ASME for publication in the JOURNAL OF ELECTRONIC PACKAGING. Manuscript received January 11, 2020; final manuscript received April 12, 2020; published online May 21, 2020. Assoc. Editor: Sreekant Narumanchi.

This manuscript has been authored by National Technology & Engineering Solutions of Sandia, LLC, under Contract No. DE-NA0003525 with the U.S. Department of Energy/National Nuclear Security Administration. The United States Government retains and the publisher, by accepting the article for publication, acknowledges that the United States Government retains a non-exclusive, paid-up, irrevocable, world-wide license to publish or reproduce the published form of this manuscript, or allow others to do so, for United States Government purposes.

However, the concurrent benefits of size reduction, high voltage operation, and high current operation are also accompanied by aggravated device self-heating. Extreme localized heat generation due to the electric field concentration near the drain-side corner of the gate structure results in intense heat fluxes and significant temperature rise [17–21].

Self-heating is detrimental to device performance and poses reliability issues. It degrades electrical performance due to the temperature dependence of the electrical properties such as electron mobility [22]. Self-heating also compromises the mechanical stability of the devices due to the induction of thermal stresses arising from the mismatch in the thermal expansion coefficients of GaN and the substrate material [23,24]. Furthermore, the combination of thermal, piezoelectric, and residual stresses can also cause electrical performance degradation due to defect creation or a critical total stress can be reached at which point there is catastrophic failure [25,26]. As such, self-heating is inherently a reliability issue which degrades performance and reduces component mean-time-to-failure [27].

Experimental analysis of both the steady-state and transient device thermal response is crucial to understand device electrothermomechanical interactions and electrical implications associated with self-heating. Moreover, accurate thermal characterization enables calibration with multiphysics models to determine peak operating temperatures which are used for lifetime assessment [27,28] and to analyze the effectiveness of thermal management solutions [29–31]. In addition, these models can be used to better understand the coupled electrothermal device physics which can be difficult or impossible to study experimentally. Therefore, it is necessary to confidently and accurately characterize the thermal response of the devices to better understand the device physics and ensure long-term and stable operation.

Several thermal characterization techniques are commonly used to quantify self-heating in electronics including infrared thermography, Raman thermometry, and thermoreflectance thermal imaging [32–37]. While infrared thermography is the most common method employed, it has been shown to underestimate the peak temperature rise [37–39]. The temporal resolution of transient infrared thermography is limited to microsecond levels, therefore, it is not capable of capturing the thermal dynamics important in hard switching applications with rapid high power dissipation in the nanosecond regime [40,41]. In contrast, Raman thermometry is very effective as a point measurement technique to determine the temperature rise in the semiconductor channel under both steady-state [32,33,42] and transient [43,44] measurement conditions. Thermoreflectance thermal imaging is also well-suited for steady-state and transient micro-electronics temperature assessment due to the abundance of metallization structures and two-dimensional mapping capabilities [34,45]. However, due to low signal-to-noise ratios, it commonly employs an iterative lock-in measurement scheme which forces synchronization of pulsed device operation and optical probing [46]. Improper use of this technique resulting from failure to fully understand the thermal dynamics of the system can result in reporting of quasi-steady-state temperature rises in the device channel which can be significantly lower than the true steady-state value.

In this work, the thermal dynamics of an AlGaIn/GaN HEMT will be studied through integrated optical probing [47] using thermoreflectance thermal imaging and Raman thermometry. A brief review of the fundamental concepts of these techniques will be given and followed by a discussion concerning proper use of thermoreflectance thermal imaging for steady-state temperature quantification. This discussion will be succeeded by complete lateral and vertical transient thermal characterization using both thermoreflectance thermal imaging and Raman thermometry. This complete transient thermal analysis allows insight to the thermal dynamics present in the operating regimes of high power switching applications and establishes a pathway to evaluate potential thermal management approaches.

## 2 Materials and Methods

Thermal characterization was performed on a single-finger AlGaIn/GaN HEMT using thermoreflectance thermal imaging and Raman thermometry. In order to optically probe the entire lateral and vertical domains of the device structure, variations of each technique were also used. Both visible and ultraviolet (UV) wavelength thermoreflectance thermal imaging were used to probe the metallization structures and GaN channel, respectively. Both standard Raman thermometry and nanoparticle-assisted Raman thermometry were used to probe the Si substrate and channel surface, respectively.

**2.1 Device Description.** The AlGaIn/GaN HEMT was grown on a 650  $\mu\text{m}$  thick Si substrate. A 4.3  $\mu\text{m}$  thick GaN buffer was grown on the Si substrate followed by a 20 nm  $\text{Al}_{0.23}\text{Ga}_{0.77}\text{N}$  barrier layer to form the 2DEG. The structure was capped with a 4 nm GaN layer and passivated with a 20 nm  $\text{SiO}_2$  layer. Ti/Al/Ni/Au (20/100/25/50 nm) Ohmic contacts were formed with e-beam evaporation followed by rapid thermal annealing at 800  $^\circ\text{C}$ . A Ni/Au (20/200 nm) Schottky gate was also formed using e-beam evaporation with a gate length of 2  $\mu\text{m}$  and a 1  $\mu\text{m}$  gate-overhang on both the drain and source sides of the gate. The source-gate and drain-gate spacings are 3  $\mu\text{m}$  and 15  $\mu\text{m}$ , respectively. The gate width is 100  $\mu\text{m}$ . Both a top-side view and a cross-sectional schematic of the device structure are shown in Fig. 1.

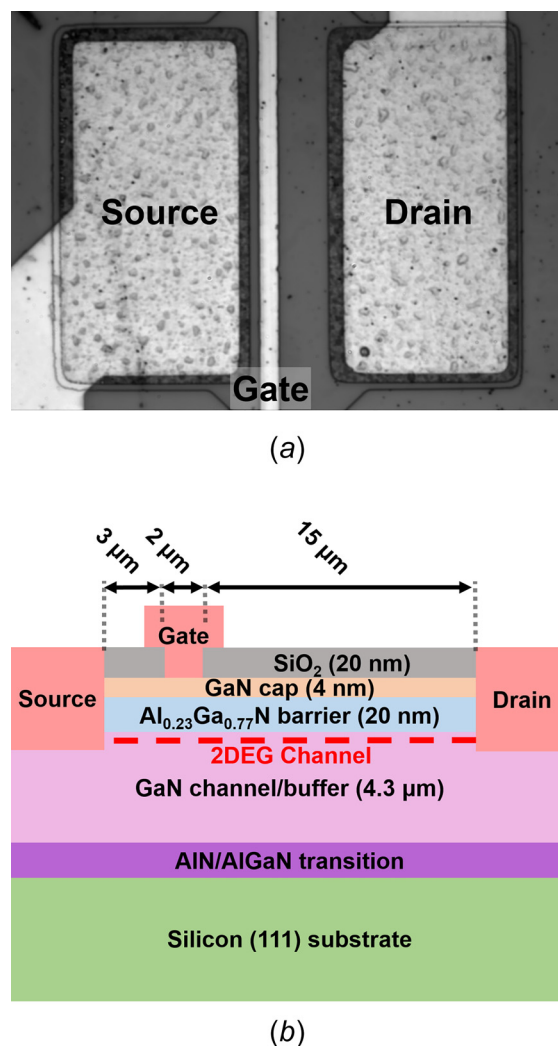


**Fig. 1** (a) Top-side and (b) cross-sectional view of the AlGaIn/GaN high electron mobility transistor analyzed in the study

**2.2 Thermoreflectance Thermal Imaging.** Thermoreflectance thermal imaging is ultimately governed by the temperature and wavelength dependence of the complex index of refraction. Experimentally, the temperature dependence of the reflectance of the material is measured using a charge coupled-device camera. This is because the complex index of refraction describes the reflectance of a material [48].

If the temperature dependence of the reflectance can be determined, the material temperature can be obtained. This relationship is established through the introduction of the thermoreflectance coefficient ( $C_{TR}$ ) defined below [46,48]:

$$C_{TR} = \frac{1}{R_0} \frac{\partial R}{\partial T} = \frac{1}{R_0} \frac{R - R_0}{T - T_0} \quad (1)$$

where  $R_0$  and  $T_0$  are the reflectance and temperature at the unpowered (cold) state and  $R$  and  $T$  are the reflectance and temperature at the powered (hot) state (Fig. 2). If the thermoreflectance coefficient is known and the reflectance at two different temperatures is measured, it follows that the temperature difference between these two states can be calculated. For example, the reflectance of the surface of a micro-electronic device can be measured at a “hot” temperature during the ON-state ( $R$ ) and at a “cold” temperature during the OFF-state ( $R_0$ ). Using the  $C_{TR}$  of the device surface and Eq. (1), the temperature rise ( $\partial T$ ) of the device surface can be calculated. As mentioned above, the complex index of refraction and thus the reflectance is also wavelength dependent; this allows for various excitation wavelengths to be tested in order to maximize the thermoreflectance coefficient for maximum measurement sensitivity.

However, the  $C_{TR}$  is still typically only on the order of  $10^{-5} \text{ K}^{-1}$  to  $10^{-3} \text{ K}^{-1}$ ; therefore, it is desirable to enhance the signal-to-noise ratio by employing a lock-in modulation scheme [46]. In this measurement scheme (Fig. 2), an electrical pulse train biasing the device causes a repeated change in reflectance. The “hot” and “cold” reflectance are repeatedly measured using a fixed LED pulse train that is synchronized with the electrical pulse train. The lock-in modulation allows the reflectance signal to be accumulated over many periods reducing the required measurement acquisition time. As such, thermoreflectance thermal imaging is an iterative measurement technique. This pulsed measurement technique can be easily transformed for transient thermal characterization by shifting the temporal location of the LED pulse

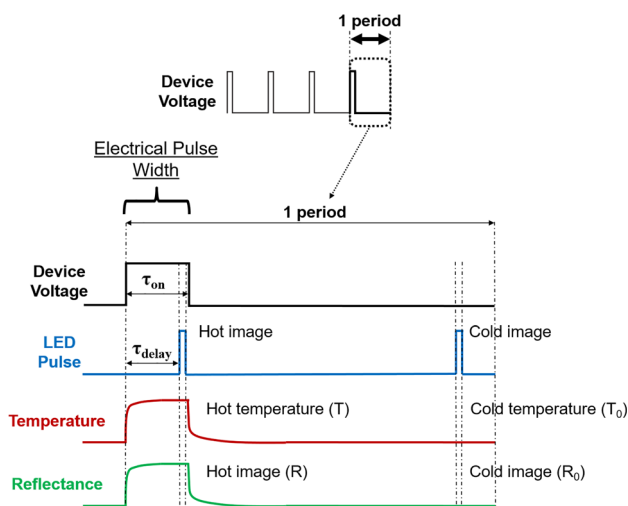


**Fig. 2** A schematic illustrating the synchronized electrical and LED pulsing in the lock-in modulation scheme employed for thermoreflectance thermal imaging. The top of the figure shows the repetitive cycling involved to accumulate the reflectance signal over many periods. The bottom of the figure highlights the pulse synchronization for one period.

( $\tau_{\text{delay}}$ ) inside the device voltage electrical pulse width ( $\tau_{\text{on}}$ ) as shown in Fig. 2.

Thermoreflectance thermal imaging is uniquely applicable for the thermal characterization of micro-electronics due to the abundance of highly reflective metallization structures. Also, by changing the LED illumination wavelength, more regions of the device can be probed. For example, the GaN channel region is transparent to visible wavelengths because the bandgap of GaN ( $\sim 3.4 \text{ eV}$ ) is greater than the corresponding photonic energy of visible wavelengths. However, ultraviolet LED illumination wavelengths such as 365 nm ( $\sim 3.4 \text{ eV}$ ) probe the GaN channel region and thus enable thermal measurements near the heat generation in the 2DEG channel (Fig. 1). Moreover, by using multiple illumination wavelengths, not only can the entire device surface be probed, but measurements results can also be validated by measuring a specific region with multiple LED illumination wavelengths.

In this study, thermoreflectance thermal imaging was conducted using a Microsanj NT-210A system equipped with a three-axis piezocontrolled stage and a  $1626 \times 1236$  pixel charge coupled-device camera. Visible 530 nm LED illumination ( $50\times$ ,  $\text{NA}=0.45$ ) was used to probe the temperature of the metal gate, drain, and source electrodes with a spatial resolution of  $\sim 600 \text{ nm}$ . Ultraviolet 365 nm LED illumination ( $40\times$ ,  $\text{NA}=0.60$ ) was used to probe the temperature of the GaN channel regions with a spatial resolution of  $\sim 300 \text{ nm}$  [49]. The temporal resolution of the thermoreflectance thermal imaging system is  $\sim 50 \text{ ns}$  which is defined by the minimum LED pulse width.

**2.3 Raman Thermometry.** Raman thermometry entails the use of Raman spectroscopy to perform temperature measurements. Raman spectroscopy uses monochromatic photonic excitation to probe the energy of the crystal lattice vibrations (phonons). Incident photons interact with the crystal lattice through scattering events. The vast majority of these scattering events are elastic: the photon incident upon the sample is emitted from the sample with no change in the photon energy (wavelength). This elastic scattering, where the incident and emitted photons have the same energy, is known as Rayleigh scattering. Much less frequently, these scattering events are inelastic: the photon incident upon the sample is emitted from the sample with either an increase or decrease in the photon energy. This inelastic scattering, where the emitted photon has either gained or lost energy with respect to the incident photon, is known as anti-Stokes or Stokes Raman scattering, respectively. The manifestation of these scattering processes in a typical Raman spectrum are shown in Fig. 3(a). As a consequence of the conservation of energy, the increase or decrease in the emitted photon energy with respect to the incident photon energy is due to the annihilation or creation of a phonon in the crystal. The difference in the incident and emitted photon energy is therefore indicative of the phonon energy (frequency, wavenumber) in the crystal [50].

There are a few effects of temperature on phonon characteristics that can be observed in Raman spectra. These include peak position shifts, peak broadening, and changes in the ratio of anti-Stokes/Stokes Raman peak intensities ( $I_{\text{as}}/I_{\text{s}}$ ) [32,42]. These phonon characteristics and the effect of temperature are shown in Fig. 3(b). If the rate of change of these characteristics with temperature is known, changes in the Raman spectra between two states can be measured and used to determine a temperature change. For example, a semiconductor material in a micro-electronic device would be measured with Raman spectroscopy during the unpowered OFF-state and during a biased ON-state. The change in the characteristics of the Raman spectra would be monitored to determine the temperature rise in the operating semiconductor device. Among the three methods for measuring temperature with Raman spectroscopy, the peak position-based method is the most common. This is because the linewidth method has large measurement uncertainty and generally lower sensitivity to temperature, and the anti-Stokes/Stokes intensity ratio method



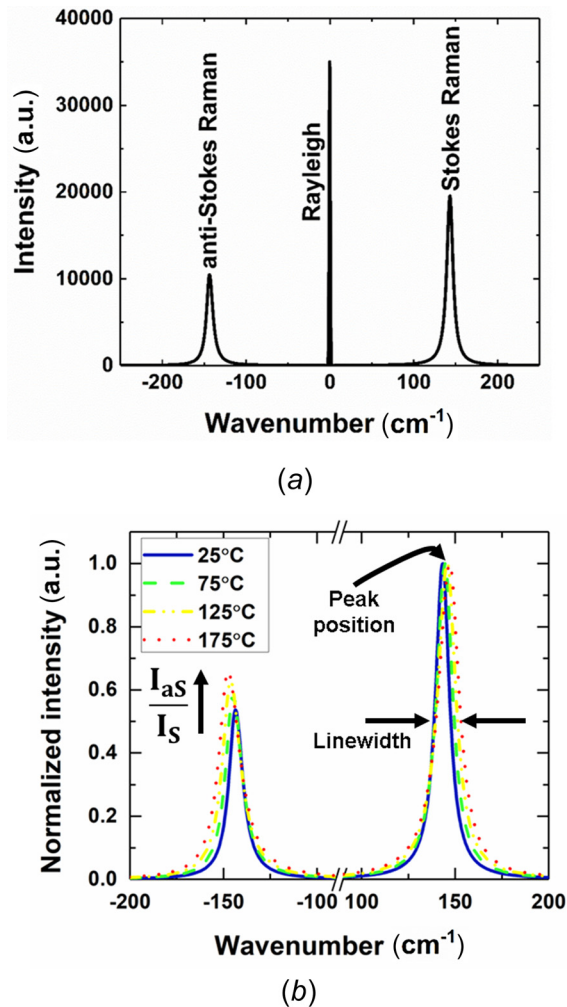


**Fig. 3** (a) A typical Raman spectrum showing (from left) anti-Stokes Raman, Rayleigh, and Stokes Raman peaks. (b) The effect of temperature on the peak position, linewidth, and anti-Stokes/Stokes intensity ratio ( $I_{aS}/I_S$ ) in the Raman spectra. The spectra shown in (b) is the same as for (a) with the exception of the Rayleigh peak which has been removed. All Raman spectra shown are of an anatase (TiO<sub>2</sub>) nanoparticle. The Raman peak observed at approximately  $\pm 145 \text{ cm}^{-1}$  is the TiO<sub>2</sub>  $E_g$  phonon mode.

requires expensive notch filters and longer acquisition times. The drawback of using the peak position-based method is that the Raman peak position is sensitive to both temperature and temperature-induced thermo-elastic stress which can lead to inaccuracies in the thermal measurement [32,42]. However, this can be overcome using specialized forms of Raman thermometry such as nanoparticle-assisted Raman thermometry which will be discussed shortly.

Similar to thermoreflectance thermal imaging, Raman thermometry is uniquely applicable for the thermal characterization of micro-electronics because it can probe the temperature of semiconductor materials. If the laser wavelength and corresponding energy are less than the bandgap of the semiconductor, there is a finite amount of depth-averaging [51]. If the laser energy is above the bandgap of the semiconductor, the surface temperature will be measured as laser absorption will occur; in this case, laser heating and photocurrent induction must be considered. While Raman spectroscopy cannot be used to directly probe metals, nanoparticle-assisted Raman thermometry can be used to indirectly probe the temperatures of metals [52]. This is because nanoparticles will be deposited on the surface of the device to be used

as temperature transducers (Fig. 4). As follows, this variation of Raman thermometry can also be used to measure the surface temperature of semiconductors whose bandgaps are greater than the Raman laser energy where depth averaging would occur. Moreover, the nanoparticles are assumed to be in thermal equilibrium with the device surface, not alter the intrinsic temperature distribution, and experience negligible thermal stress. This facilitates the use of peak position-based methods for thermal characterization as there are no stress effects on the nanoparticle Raman peak positions.

The standard Raman spectrometer can be used for steady-state thermal characterization, but with additional equipment Raman thermometry can be used for transient measurements (Fig. 5). The transient measurement experimental setup in Fig. 5 adopts a lock-in modulation scheme similar to thermoreflectance thermal imaging in which the electrical and laser pulse trains are synchronized and the signal accumulates over many periods. Using the experimental setup in Fig. 5, a temporal resolution of 15 ns was achieved and used in this study.

Both nanoparticle-assisted and standard Raman thermometry were used to probe the surface and Si substrate surface temperatures of the AlGaIn/GaN HEMT, respectively. The surface temperature was probed using anatase titanium dioxide (TiO<sub>2</sub>) nanoparticles (99.98% purity) [52]. Raman thermometry was performed using a Horiba LabRAM HR Evolution spectrometer in a 180 deg backscattering configuration. The system is equipped with 532 nm laser excitation (2.33 eV) and measurements were performed with a long working distance 50 $\times$  objective (NA = 0.45). For standard Raman thermometry, this experimental setup offers a spatial resolution of  $\sim 600 \text{ nm}$ ; for nanoparticle-assisted Raman thermometry, the spatial resolution is limited by the size of the TiO<sub>2</sub> nanoparticles. To minimize the laser heating effect in the Si substrate and TiO<sub>2</sub> nanoparticles, a low laser power ( $\sim 1 \text{ mW}$ ) was adopted. Systematic error was corrected using a reference mercury emission line at 546 nm.

### 3 Results and Discussion

Since thermoreflectance thermal imaging is a pulsed measurement technique, it is important that the user ensures that the device under test is allowed to reach a true steady-state condition. The device electrical pulse width ( $\tau_{on}$ ) set as a measurement input parameter for a fixed duty cycle (Fig. 2) should never be arbitrarily chosen; this should be determined with transient thermal characterization to analyze the transient thermal response of the device using various device electrical pulse widths. The electrical pulse width should be continually increased until there are no more increases in the temperature measured at the end of the electrical pulse ( $T$ , Fig. 2). Also, the duty cycle selected should be low enough to ensure that the entire material stack has sufficient time to cool to the reference base temperature ( $T_0$ , Fig. 2) before the reference reflectance signal ( $R_0$ , Fig. 2) is measured. To determine the electrical pulse width, a small region of interest (ROI) is often selected on an important feature of the device to determine the pulse width at which no further increases in temperature are observed with increasing electrical pulse width; for the AlGaIn/GaN HEMT used in this study, this feature would generally be the gate contact due to the localization of heat generation at the drain-side corner of the gate [17,19,53]. However, another important consideration is lateral heat spreading. While the gate may approach its steady-state value at a given pulse width, other features of the device may not have reached the steady-state temperature. This is due to the thermal lag arising from the electrical pulse width dependent thermal penetration length, i.e., the lateral extent of heat spreading where temperature rise above the base plate temperature of the device under test (DUT) occurs. This will be demonstrated using the AlGaIn/GaN HEMT shown in Fig. 1 for electrical pulse widths of 10  $\mu\text{s}$ , 100  $\mu\text{s}$ , and 1000  $\mu\text{s}$  (Fig. 6). The AlGaIn/GaN HEMT was biased to operate with a power density of  $P = 6 \text{ W/mm}^2$  for all electrical pulse widths. The drain-

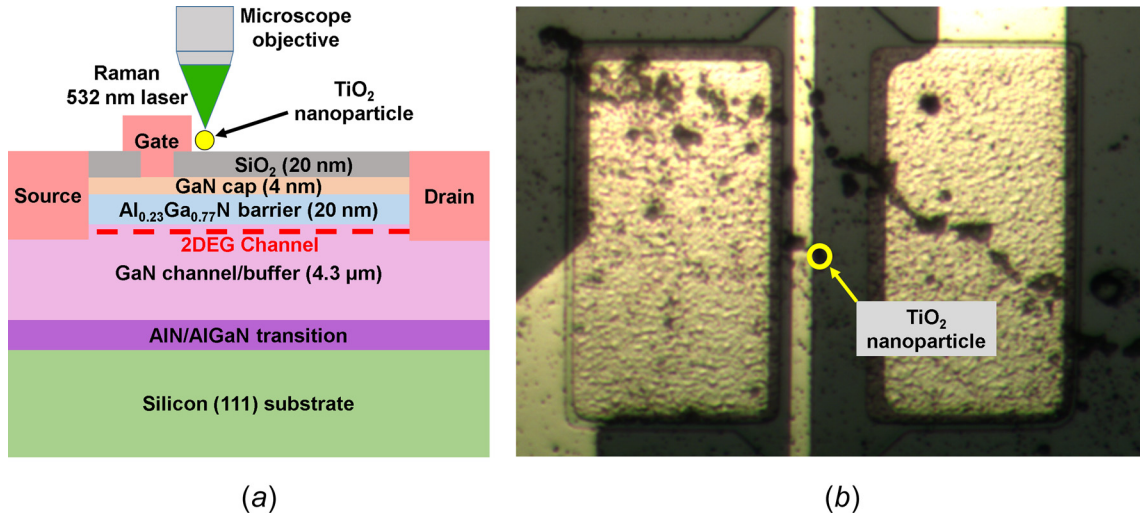


**Fig. 4** (a) Schematic of nanoparticle-assisted Raman thermometry showing probing of the TiO<sub>2</sub> nanoparticle on the device surface. (b) Optical image of TiO<sub>2</sub> nanoparticles deposited on the AlGaIn/GaN HEMT. The sphere and circular outline in (a) and (b), respectively, indicate the location of the TiO<sub>2</sub> nanoparticle.

source voltage ( $V_{DS}$ ) was held constant at 28 V while the gate voltage ( $V_{GS}$ ) was adjusted to maintain constant power density.

The transient thermal response of the AlGaIn/GaN HEMT for each electrical pulse width is shown in Fig. 6 for ROIs on the gate and drain contacts. The temperature rise for each ROI shown is normalized with respect to the steady-state temperature rise for the respective ROI (i.e.,  $T_{Gate}$ ,  $10 \mu s / T_{Gate, steady-state}$ ). For the electrical pulse width of 10 μs, it can be seen that neither the gate nor the drain contacts reach their steady-state value. Furthermore, while the gate contact reaches almost 90% of its steady-state value in 10 μs, the drain contact only reaches approximately 50% of its steady-state value due to the thermal lag imposed by the finite thermal penetration length. For the electrical pulse width of 100 μs, the thermal penetration length has increased and the thermal lag between the gate and drain contacts has reduced significantly. The gate and drain ROIs have respectively reached approximately

95% and 90% of their steady-state temperature rise. It should be noted that if only the gate ROI was used, it would appear that the device has reached a steady-state condition when in fact this is only a quasi-steady-state condition in the vicinity of the heat source. As can be clearly seen from the drain ROI, the true device steady-state condition has not been reached. When the electrical pulse width is increased to 1000 μs, it is finally possible to observe that all features on the device surface have reached the true steady-state condition. Careful consideration should be given to ensure that all regions of the device have reached a true steady-state condition as shown in Fig. 6.

An extreme case demonstrating poor selection of the electrical pulse width is shown in Fig. 7. The AlGaIn/GaN HEMT was biased at the same conditions as in Fig. 6 ( $P = 6 \text{ W/mm}$ ,  $V_{DS} = 28 \text{ V}$ ), however, the electrical pulse width was set to 1 μs and measured with a temporal resolution of approximately 50 ns. Under this electrical pulse width condition, the gate contact can

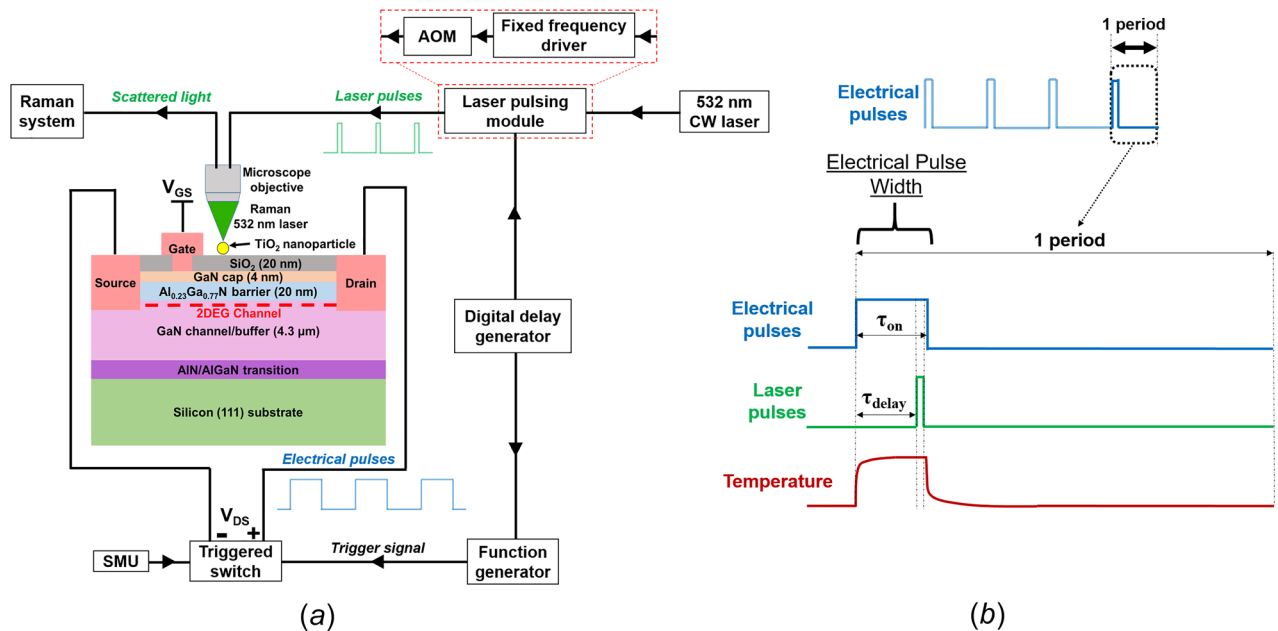


**Fig. 5** The (a) experimental setup and (b) synchronized pulsing scheme used to enable transient measurements using Raman thermometry

be seen to clearly demonstrate significant temperature rise ( $\sim 40^\circ\text{C}$ ), yet the drain contact shows absolutely no temperature rise. If evaluating the steady-state thermal response of the device, this thermal characterization would be meaningless, but for some

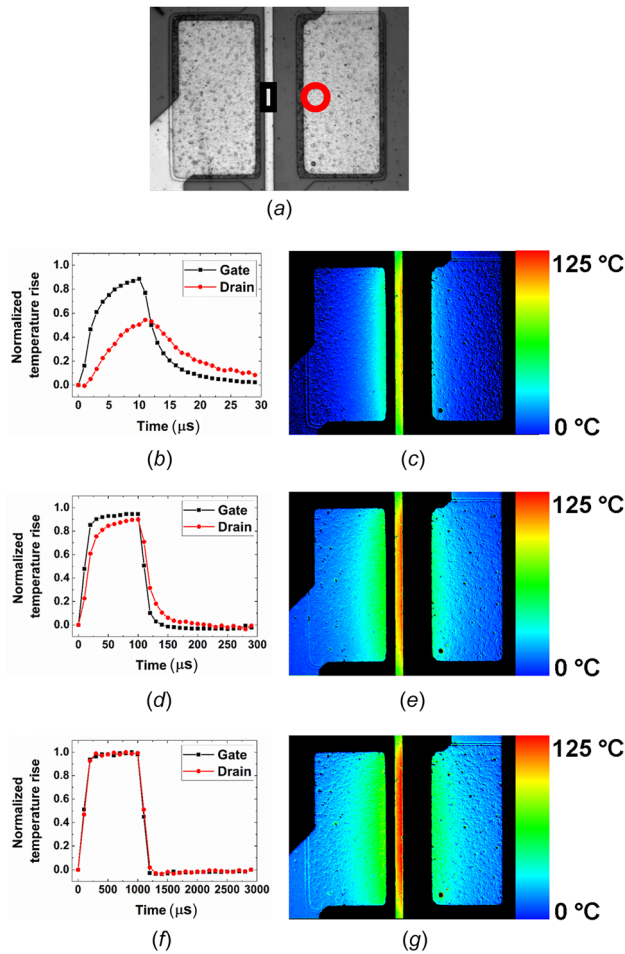


**Fig. 6** (a) Top-side view of the device highlighting the gate (square) and drain (circle) regions of interest during the transient thermal characterization. (b), (d), and (f) The transient temperature rise of the gate and drain regions from (a) normalized with respect to the steady-state temperature rise of the respective region for electrical pulse widths of 10  $\mu\text{s}$ , 100  $\mu\text{s}$ , and 1000  $\mu\text{s}$ . (c), (e), and (g) Thermal image of the device surface using visible 530 nm thermoreflectance thermal imaging for electrical pulse widths of 10  $\mu\text{s}$ , 100  $\mu\text{s}$ , and 1000  $\mu\text{s}$  for  $P = 6 \text{ W/mm}$  ( $V_{\text{DS}} = 28 \text{ V}$ ).

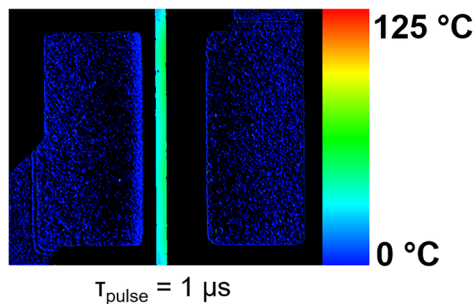


**Fig. 7** A thermal image of the device surface using thermoreflectance thermal imaging with 530 nm illumination. The thermal map was obtained for an electrical pulse width of 1  $\mu\text{s}$  and an LED pulse width of 50 ns.

switching applications [54] where there are fast transient heating events, this thermal analysis can be quite useful and insightful.

Using the transient measurement capabilities of both visible and ultraviolet thermoreflectance thermal imaging, the transient temperature response of the entire device surface, i.e., the lateral thermal dynamics of the device, can be determined. The Microsanj NT-210A thermoreflectance imaging system allows a temporal resolution down to 50 ns. The thermal analysis can be extended using the developed transient Raman thermometry setup (Fig. 5) to enable integrated optical probing through the material stack thickness, i.e., the vertical thermal dynamics, of the AlGaIn/GaN HEMT with a temporal resolution down to 15 ns. Using 365 nm and 530 nm LED illumination with thermoreflectance thermal imaging to respectively probe the GaN channel and metal contacts (gate, drain, and source electrodes) and nanoparticle-assisted and standard Raman thermometry to respectively probe the  $\text{TiO}_2$  nanoparticle (surface) and Si substrate surface, the multi-dimensional thermal response of the device can be determined and analyzed. These results are shown in Fig. 8 for the AlGaIn/GaN HEMT operating with a power density of  $P = 6 \text{ W/mm}$  at  $V_{\text{DS}} = 28 \text{ V}$ . For measurement of the GaN channel and metal contacts with 365 nm and 530 nm LED illumination, two-dimensional point-by-point  $C_{\text{TR}}$  calibration maps were used. For 365 nm

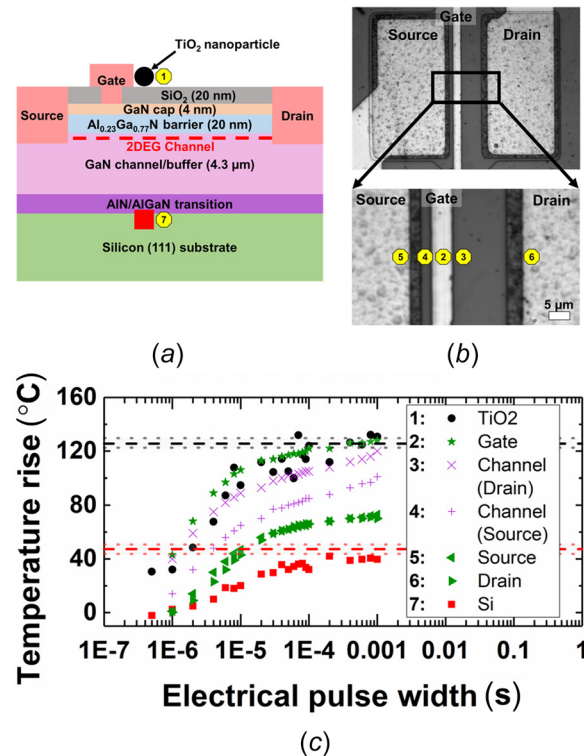


**Fig. 8** (a) Cross-sectional device schematic showing locations measured using nanoparticle-assisted and standard Raman thermometry; the former probes the  $\text{TiO}_2$  nanoparticle (sphere, 1) and the latter probes the Si substrate surface (square, 7). (b) Top-side view of the device showing locations measured using UV 365 nm (3, 4) and visible 530 nm (2, 5, 6) thermoreflectance thermal imaging. (c) The temperature rise as a function of electrical pulse width for the seven regions of interest in (a) and (b). The top and bottom long-dash lines represent the steady-state temperature rise of the  $\text{TiO}_2$  nanoparticle and Si substrate surface, respectively. The short-dash lines represent the uncertainty associated with the measurements. As a result of long acquisition times during transient measurements, single measurements were obtained at each electrical pulse width, and thus no uncertainty analysis was completed for these measurements; however, typical uncertainties associated with these techniques are on the order of  $\pm 1\text{--}5^\circ\text{C}$ .



illumination of the GaN channel, the average  $C_{TR}$  was approximately  $-2.8 \times 10^{-3} \text{ K}^{-1}$ , and for 530 nm illumination of the metal contacts, the average  $C_{TR}$  was approximately  $-1.5 \times 10^{-4} \text{ K}^{-1}$ .

For the maximum electrical pulse width (1000  $\mu\text{s}$ ), the temperature rise in all regions of the device is seen to reach the steady-state value. The maximum temperature rises in the device are seen at the gate, drain-side of the channel, and the  $\text{TiO}_2$  nanoparticle acting as a surface temperature transducer on the drain-side of the gate (Fig. 8). This is expected because these three locations are all nearest to the localized heat generation which occurs at the drain-side corner of the gate in the GaN channel layer. The temperature rise measured on the drain-side of the channel is observed to be slightly less than the temperature rise measured for the gate and  $\text{TiO}_2$  nanoparticle. This discrepancy is due to edge effects occurring at the gate field plate edge [55] and finite distance between the ROI and the drain-side edge of the gate where Joule heating is concentrated [17,19,53]. The source-side channel temperature rise is observed to be less than on the drain-side which is understandable since the source-side is further from the localized heat generation on the drain-side edge of the gate. Because the drain and source Ohmic contacts are the farthest from the heat generation and the Si substrate acts as a heat sink underneath the GaN, these regions are observed to have the lowest temperature rises.

As the electrical pulse width is gradually decreased, the temperature rise in all regions is seen to decrease. While the power density remains constant, reducing the electrical pulse width results in less averaged power/heat generation. As the electrical pulse width is continually decreased, a transient regime ( $\leq 1 \mu\text{s}$ ) is reached where there is almost no measurable temperature rise in the drain and source Ohmic contacts or the Si substrate surface. This is because (i) the finite thermal penetration length from the heat generation source at the drain-side corner of the gate has now been reduced to a length scale less than or equal to the gate-drain and gate-source contact spacings, and (ii) the thermal penetration depth has been reduced to a length scale less than the GaN channel/buffer layer thickness. Therefore, from the integrated optical probing of the device thermal dynamics, a thermal penetration length of approximately 4–5  $\mu\text{m}$  is observed at an electrical pulse width of 1  $\mu\text{s}$  (10% duty cycle, 10  $\mu\text{s}$  period). Due to limitations on the LED pulse width ( $\sim 50 \text{ ns}$ ) using thermoreflectance thermal imaging, the minimum electrical pulse width for which the thermal response could be measured was 1  $\mu\text{s}$ . However, using transient Raman thermometry with a temporal resolution of 15 ns, the electrical pulse width can be further reduced. With an electrical pulse width of 500 ns, no heating is observed in the Si substrate while a temperature rise of approximately 30  $^\circ\text{C}$  is measured for

the  $\text{TiO}_2$  nanoparticle at the device surface. This quantification further solidifies the concept of the finite thermal penetration depth which has now been reduced to less than the thickness of the GaN channel/buffer ( $\sim 4.3 \mu\text{m}$ ) for a 500 ns electrical pulse width.

#### 4 Conclusion

Thermoreflectance thermal imaging and Raman thermometry were used to probe the multidimensional thermal dynamics of an AlGaIn/GaN HEMT. The use of both visible and ultraviolet thermoreflectance thermal imaging allows measurement of the metal contacts and semiconductor channel regions, respectively. As a result, the frequency dependent thermal penetration length for a given device surface geometry can be experimentally determined. In combination with standard and nanoparticle-assisted Raman thermometry, it is also possible to probe the vertical thermal dynamics of the device. From Fig. 8 it can be seen that as the pulse width is decreased, the thermal penetration depth eventually becomes less than the thickness of the GaN channel/buffer layer. This indicates that for certain power switching applications with fast transient heating events, the role of the substrate in thermal management could be insignificant. In this case, the substrate can be selected to optimize the GaN buffer/channel layer crystalline quality. This would allow for increased mobility and thermal conductivity, improving both electrical and thermal device performance.

The integrated optical probing of the thermal dynamics of the AlGaIn/GaN HEMT can also be extended in order to understand the thermal dynamics of emerging ultrawide bandgap (UWBG) device technologies such as  $\text{Al}_x\text{Ga}_{1-x}\text{N}$  and  $\text{Ga}_2\text{O}_3$  [56–61]. Since the thermal penetration length and depth are proportional to the square root of the thermal conductivity [62], the thermal response times of these UWBG device technologies are expected to increase. To demonstrate, an  $\text{Al}_{0.45}\text{Ga}_{0.55}\text{N}/\text{Al}_{0.30}\text{Ga}_{0.70}\text{N}$  HEMT [58] and an AlGaIn/GaN HEMT (same device die as in this study) with similar device geometries ( $L_{\text{gate}} = 2 \mu\text{m}$ ,  $L_{\text{gate-drain}} = L_{\text{gate-source}} = 4 \mu\text{m}$ ) were measured using thermoreflectance thermal imaging (530 nm). The electrical pulse width was varied from 1  $\mu\text{s}$  to 60 s (steady-state) using a 10% duty cycle (Fig. 9). The steady-state temperatures of each device feature (gate and drain) were used to normalize the temperature rises as a function of electrical pulse width. As shown in Fig. 9, the thermal time constants (time to reach  $\sim 63\%$  of the steady-state temperature rise) of the gate/drain contacts were  $\sim 3/\sim 10 \mu\text{s}$  and  $\sim 30/\sim 300 \mu\text{s}$  for the AlGaIn/GaN and  $\text{Al}_{0.45}\text{Ga}_{0.55}\text{N}/\text{Al}_{0.30}\text{Ga}_{0.70}\text{N}$  HEMTs, respectively. The slower thermal response can also be seen qualitatively by the systematic shift in the normalized temperature rises of the  $\text{Al}_{0.45}\text{Ga}_{0.55}\text{N}/\text{Al}_{0.30}\text{Ga}_{0.70}\text{N}$  HEMT as compared to the AlGaIn/GaN HEMT. Therefore, for switching applications with fast transient heating events, thermal obstacles resulting from increased thermal resistances can be alleviated allowing the performance benefits from the improved electrical properties of next generation UWBG materials to be realized. Furthermore, this comparison was performed under room temperature conditions; however, while the thermal conductivity of GaN decreases at increased base temperature conditions, the relative insensitivity of the thermal conductivity of  $\text{Al}_x\text{Ga}_{1-x}\text{N}$  [63] can allow for relatively temperature independent operation. This also highlights the possible advantages that UWBG materials such as AlGaIn can have for high temperature and extreme environment applications.

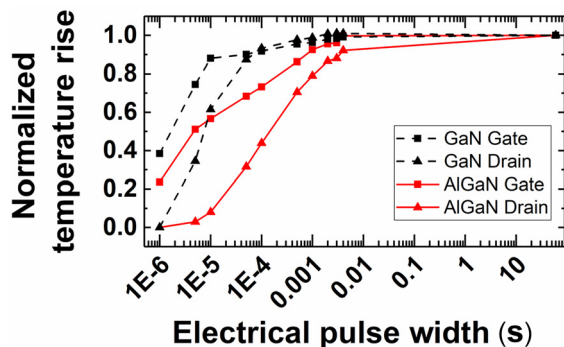


Fig. 9 Normalized temperature rise of the gate (square symbols) and drain (triangle symbols) contacts as a function of electrical pulse width for an AlGaIn/GaN HEMT (dashed line) and an  $\text{Al}_{0.45}\text{Ga}_{0.55}\text{N}/\text{Al}_{0.30}\text{Ga}_{0.70}\text{N}$  HEMT (solid line) operating with a power density of  $P = 1.6 \text{ W/mm}^2$ . The steady-state (60 s) temperature rise of the gate and drain contacts of the AlGaIn/GaN HEMT were 24  $^\circ\text{C}$  and 8  $^\circ\text{C}$ , respectively. The steady-state temperature rise of the gate and drain contacts of the  $\text{Al}_{0.45}\text{Ga}_{0.55}\text{N}/\text{Al}_{0.30}\text{Ga}_{0.70}\text{N}$  HEMT were 68  $^\circ\text{C}$  and 34  $^\circ\text{C}$ , respectively.

#### Acknowledgment

Funding for efforts by the Pennsylvania State University was provided by the AFOSR Young Investigator Program (Grant No. FA9550-17-1-0141, Program Officers: Dr. Michael Kendra and Dr. Brett Pokines, also monitored by Dr. Kenneth Goretta) and the National Science Foundation under Grant No. CBET-1934482. Efforts by Hongik University were supported by the National Research Foundation of Korea (NRF) grant funded by the Korea

government (MSIT) (No. 2016R1A1B4010474). This work was supported by the Laboratory Directed Research and Development Program at Sandia National Laboratories. Sandia National Laboratories is a multimission laboratory managed and operated by National Technology & Engineering Solutions of Sandia, LLC, a wholly owned subsidiary of Honeywell International Inc., for the U.S. Department of Energy's National Nuclear Security Administration under Contract No. DE-NA0003525. This paper describes objective technical results and analysis. Any subjective views or opinions that might be expressed in the paper do not necessarily represent the views of the U.S. Department of Energy or the United States Government.

## Funding Data

- Pennsylvania State University was provided by the AFOSR Young Investigator Program (Grant No. FA9550-17-1-0141, Program Officers: Dr. Michael Kendra and Dr. Brett Pokines, also monitored by Dr. Kenneth Goretta) (Funder ID: 10.13039/100000181).
- National Science Foundation under Grant No. CBET-1934482 (Funder ID: 10.13039/100000001).
- Hongik University were supported by the National Research Foundation of Korea (NRF) grant funded by the Korea government (MSIT) (No. 2016R1A1B4010474; Funder ID: 10.13039/501100003725).
- Laboratory Directed Research and Development Program at Sandia National Laboratories (Funder ID: 10.13039/100006234).
- U.S. Department of Energy's National Nuclear Security Administration under Contract No. DE-NA0003525 (Funder ID: 10.13039/100006168).
- Division of Chemical, Bioengineering, Environmental, and Transport Systems (Funder ID: 10.13039/100000146).

## Nomenclature

- $C_{TR}$  = thermorefectance coefficient  
 $E_G$  = bandgap energy  
 $I_{as}/I_s$  = anti-Stokes/Stokes Raman intensity ratio  
 $P$  = power density  
 $V_{DS}$  = drain-source voltage  
 $V_{GS}$  = gate-source voltage  
 $\tau_{\text{delay}}$  = LED pulse time delay  
 $\tau_{\text{on}}$  = electrical pulse width  
 2DEG = two-dimensional electron gas

## References

- [1] Mishra, U. K., Shen, L., Kazior, T. E., and Wu, Y., 2008, "GaN-Based RF Power Devices and Amplifiers," *Proc. IEEE*, **96**(2), pp. 287–305.
- [2] Komiak, J. J., 2015, "GaN HEMT: Dominant Force in High-Frequency Solid-State Power Amplifiers," *IEEE Microw. Mag.*, **16**(3), pp. 97–105.
- [3] Trew, R. J., Shin, M. W., and Gatto, V., 1997, "High Power Applications for GaN-Based Devices," *Solid State Electron.*, **41**(10), pp. 1561–1567.
- [4] Chen, K. J., Haberlen, O., Lidow, A., Tsai, C. L., Ueda, T., Uemoto, Y., and Wu, Y., 2017, "GaN-on-Si Power Technology: Devices and Applications," *IEEE Trans. Electron Devices*, **64**(3), pp. 779–795.
- [5] Palacios, T., Chakraborty, A., Rajan, S., Poblentz, C., Keller, S., DenBaars, S. P., Speck, J. S., and Mishra, U. K., 2005, "High-Power AlGaIn/GaN HEMTs for Ka-Band Applications," *IEEE Electron Device Lett.*, **26**(11), pp. 781–783.
- [6] Millan, J., Godignon, P., Perpina, X., Perez-Tomas, A., and Rebollo, J., 2014, "A Survey of Wide Bandgap Power Semiconductor Devices," *IEEE Trans. Power Electron.*, **29**(5), pp. 2155–2163.
- [7] Pengelly, R. S., Wood, S. M., Milligan, J. W., Sheppard, S. T., and Pribble, W. L., 2012, "A Review of GaN on SiC High Electron-Mobility Power Transistors and MMICs," *IEEE Trans. Microwave Theory Tech.*, **60**(6), pp. 1764–1783.
- [8] Ozpineci, B., and Tolbert, L. M., 2003, "Comparison of Wide-Bandgap Semiconductors for Power Electronics Applications," Oak Ridge National Laboratory, Oak Ridge, TN, Report No. ORNL/TM-2003/257.
- [9] Shur, M., and Davis, R. F., 2004, *GaN-Based Materials and Devices: Growth, Fabrication, Characterization and Performance*, World Scientific, Singapore.
- [10] Levinshtein, M. E., Rumyantsev, S. L., and Shur, M. S., 2001, *Properties of Advanced Semiconductor Materials: GaN, AlN, InN, BN, SiC, SiGe*, Wiley, New York.
- [11] Flack, T. J., Pushpakaran, B. N., and Bayne, S. B., 2016, "GaN Technology for Power Electronic Applications: A Review," *J. Electron. Mater.*, **45**(6), pp. 2673–2682.
- [12] Ambacher, O., Smart, J., Shealy, J. R., Weimann, N. G., Chu, K., Murphy, M., Schaff, W. J., Eastman, L. F., Dimitrov, R., Wittmer, L., Stutzmann, M., Rieger, W., and Hilsenbeck, J., 1999, "Two-Dimensional Electron Gases Induced by Spontaneous and Piezoelectric Polarization Charges in N- and Ga-Face AlGaIn/GaN Heterostructures," *J. Appl. Phys.*, **85**(6), pp. 3222–3233.
- [13] Cimalla, V., Pezoldt, J., and Ambacher, O., 2007, "Group III Nitride and SiC Based MEMS and NEMS: Materials Properties, Technology and Applications," *J. Phys. D: Appl. Phys.*, **40**(20), pp. 6386–6434.
- [14] Mitova, R., Ghosh, R., Mhaskar, U., Klikic, D., Wang, M. X., and Dentella, A., 2014, "Investigations of 600-V GaN HEMT and GaN Diode for Power Converter Applications," *IEEE Trans. Power Electron.*, **29**(5), pp. 2441–2452.
- [15] Wu, Y., Jacob-Mitos, M., Moore, M. L., and Heikman, S., 2008, "A 97.8% Efficient GaN HEMT Boost Converter With 300-W Output Power at 1 MHz," *IEEE Electron Device Lett.*, **29**(8), pp. 824–826.
- [16] Zhang, N., Mehrotra, V., Chandrasekaran, S., Moran, B., Shen, L., Mishra, U., Etzkorn, E., and Clarke, D., 2004, "Large Area GaN HEMT Power Devices for Power Electronic Applications: Switching and Temperature Characteristics," *PESC Record—IEEE Annual Power Electronics Specialists Conference*, Acapulco, Mexico, June 15–19, pp. 233–237.
- [17] Choi, S., Heller, E. R., Dorsey, D., Vetury, R., and Graham, S., 2013, "The Impact of Bias Conditions on Self-Heating in AlGaIn/GaN HEMTs," *IEEE Trans. Electron Devices*, **60**(1), pp. 159–162.
- [18] Wang, X. D., Hu, W. D., Chen, X. S., and Lu, W., 2012, "The Study of Self-Heating and Hot-Electron Effects for AlGaIn/GaN Double-Channel HEMTs," *IEEE Trans. Electron Devices*, **59**(5), pp. 1393–1401.
- [19] Heller, E., Choi, S., Dorsey, D., Vetury, R., and Graham, S., 2013, "Electrical and Structural Dependence of Operating Temperature of AlGaIn/GaN HEMTs," *Microelectron. Reliab.*, **53**(6), pp. 872–877.
- [20] Si, J., Wei, J., Chen, W., and Zhang, B., 2013, "Electric Field Distribution Around Drain-Side Gate Edge in AlGaIn/GaN HEMTs: Analytical Approach," *IEEE Trans. Electron Devices*, **60**(10), pp. 3223–3229.
- [21] Sridharan, S., Venkatachalam, A., and Yoder, P. D., 2008, "Electrothermal Analysis of AlGaIn/GaN High Electron Mobility Transistors," *J. Comput. Electron.*, **7**, pp. 236–239.
- [22] Lisesivdin, S. B., Acar, S., Kasap, M., Ozcelik, S., Gokden, S., and Ozbay, E., 2007, "Scattering Analysis of 2DEG Carrier Extracted by QMSA in Undoped Al<sub>0.25</sub>Ga<sub>0.75</sub>N/GaN Heterostructures," *Semicond. Sci. Technol.*, **22**(5), pp. 543–548.
- [23] Qu, S., Li, S., Peng, Y., Zhu, X., Hu, X., Wang, C., Chen, X., Gao, Y., and Xu, X., 2010, "Influence of the Growth Temperature of AlN Buffer on the Quality and Stress of GaN Films Grown on 6H-SiC Substrate by MOVPE," *J. Alloys Compd.*, **502**(2), pp. 417–422.
- [24] Ishida, M., Ueda, T., Tanaka, T., and Ueda, D., 2013, "GaN on Si Technologies for Power Switching Devices," *IEEE Trans. Electron Devices*, **60**(10), pp. 3053–3059.
- [25] Choi, S., Heller, E., Dorsey, D., Vetury, R., and Graham, S., 2013, "The Impact of Mechanical Stress on the Degradation of AlGaIn/GaN High Electron Mobility Transistors," *J. Appl. Phys.*, **114**(16), p. 164501.
- [26] del Alamo, J. A., and Joh, J., 2009, "GaN HEMT Reliability," *Microelectron. Reliab.*, **49**(9–11), pp. 1200–1206.
- [27] Heller, E. R., 2008, "Simulation of Life Testing Procedures for Estimating Long-Term Degradation and Lifetime of AlGaIn/GaN HEMTs," *IEEE Trans. Electron Devices*, **55**(10), pp. 2554–2560.
- [28] Pomeroy, J. W., Uren, M. J., Lambert, B., and Kuball, M., 2015, "Operating Channel Temperature in GaN HEMTs: DC Versus RF Accelerated Life Testing," *Microelectron. Reliab.*, **55**(12), pp. 2505–2510.
- [29] Choi, S., Peake, G. M., Keeler, G. A., Geib, K. M., Briggs, R. D., Beechem, T. E., Shaffer, R. A., Clevenger, J., Patrizi, G. A., Klem, J. F., Tauke-Pedretti, A., and Nordquist, C. D., 2016, "Thermal Design and Characterization of Heterogeneously Integrated InGaP/GaAs HBTs," *IEEE Trans. Compon. Packag. Manuf. Technol.*, **6**(5), pp. 740–748.
- [30] Yan, Z., Liu, G., Khan, J. M., and Balandin, A. A., 2012, "Graphene Quilts for Thermal Management of High-Power GaN Transistors," *Nat. Commun.*, **3**, pp. 827–828.
- [31] Won, Y., Cho, J., Agonafer, D., Asheghi, M., and Goodson, K. E., 2013, "Cooling Limits for GaN HEMT Technology," Technical Digest—IEEE Compound Semiconductor Integrated Circuit Symposium (CSIC), Monterey, CA, Oct. 13–16, pp. 1–5.
- [32] Choi, S., Heller, E. R., Dorsey, D., Vetury, R., and Graham, S., 2013, "Thermometry of AlGaIn/GaN HEMTs Using Multispectral Raman Features," *IEEE Trans. Electron Devices*, **60**(6), pp. 1898–1904.
- [33] Kuball, M., Hayes, J. M., Uren, M. J., Martin, T., Birbeck, J. C. H., Balmer, R. S., and Hughes, B. T., 2002, "Measurement of Temperature in Active High-Power AlGaIn/GaN HFETs Using Raman Spectroscopy," *IEEE Electron Device Lett.*, **23**(1), pp. 7–9.
- [34] Maize, K., Pavlidis, G., Heller, E., Yates, L., Kendig, D., Graham, S., and Shakouri, A., 2014, "High Resolution Thermal Characterization and Simulation of Power AlGaIn/GaN HEMTs Using Micro-Raman Thermography and 800 Pico-second Transient Thermorefectance Imaging," Technical Digest—IEEE Compound Semiconductor Integrated Circuit Symposium (CSIC), La Jolla, CA, Oct. 19–22, pp. 1–8.
- [35] Pavlidis, G., Kendig, D., Heller, E. R., and Graham, S., 2018, "Transient Thermal Characterization of AlGaIn/GaN HEMTs Under Pulsed Biasing," *IEEE Trans. Electron Devices*, **65**(5), pp. 1753–1758.



- [36] Mitani, E., Aojima, M., and Sano, S., 2007, "A KW-Class AlGaIn/GaN HEMT Pallet Amplifier for S-Band High Power Application," *European Microwave Week 2007 Conference Proceedings, EuMW 2007—Second European Microwave Integrated Circuits Conference (EuMIC)*, Munich, Germany, Oct. 8–10, pp. 176–179.
- [37] Sarua, A., Kuball, M., Uren, M. J., Martin, T., Hilton, K. P., and Balmer, R. S., 2006, "Integrated Micro-Raman/Infrared Thermography Probe for Monitoring of Self-Heating in AlGaIn/GaN Transistor Structures," *IEEE Trans. Electron Devices*, **53**(10), pp. 2438–2447.
- [38] Yazawa, K., Kendig, D., and Shakouri, A., 2015, "Thermal Imaging Characterization for High Frequency and High Power Devices," *International Conference on Electronic Packaging and iMAPS All Asia Conference of ICEP-IAAC 2015—2015*, Kyoto, Japan, Apr. 14–17, pp. 395–400.
- [39] Killat, N., Kuball, M., Chou, T. M., Chowdhury, U., and Jimenez, J., 2010, "Temperature Assessment of AlGaIn/GaN HEMTs: A Comparative Study by Raman, Electrical and IR Thermography," *Proceedings of IEEE International Reliability Physics Symposium*, Anaheim, CA, May 2–6, pp. 528–531.
- [40] Huang, X., Li, Q., Liu, Z., and Lee, F. C., 2014, "Analytical Loss Model of High Voltage GaN HEMT in Cascode Configuration," *IEEE Trans. Power Electron.*, **29**(5), pp. 2208–2219.
- [41] Nakajima, A., Takao, K., and Ohashi, H., 2013, "GaN Power Transistor Modeling for High-Speed Converter Circuit Design," *IEEE Trans. Electron Devices*, **60**(2), pp. 646–652.
- [42] Beechem, T., Christensen, A., Graham, S., and Green, D., 2008, "Micro-Raman Thermometry in the Presence of Complex Stresses in GaN Devices," *J. Appl. Phys.*, **103**(12), p. 124501.
- [43] Riedel, G. J., Pomeroy, J. W., Hilton, K. P., Maclean, J. O., Wallis, D. J., Uren, M. J., Martin, T., and Kuball, M., 2008, "Nanosecond Timescale Thermal Dynamics of AlGaIn/GaN Electronic Devices," *IEEE Electron Device Lett.*, **29**(5), pp. 416–418.
- [44] Kuball, M., Riedel, G. J., Pomeroy, J. W., Sarua, A., Uren, M. J., Martin, T., Hilton, K. P., Maclean, J. O., and Wallis, D. J., 2007, "Time-Resolved Temperature Measurement of AlGaIn/GaN Electronic Devices Using Micro-Raman Spectroscopy," *IEEE Electron Device Lett.*, **28**(2), pp. 86–89.
- [45] Maize, K., Heller, E., Dorsey, D., and Shakouri, A., 2012, "Thermoreflectance CCD Imaging of Self Heating in AlGaIn/GaN High Electron Mobility Power Transistors at High Drain Voltage," *Annual IEEE Semiconductor Thermal Measurement and Management Symposium*, San Jose, CA, Mar. 18–22, pp. 173–181.
- [46] Kendig, D., Tay, A., and Shakouri, A., 2016, "Thermal Analysis of Advanced Microelectronic Devices Using Thermoreflectance Thermography," *22nd International Workshop on Thermal Investigations of ICs and Systems (THERMINIC)*, Budapest, Hungary, Sept. 21–23, pp. 21–23.
- [47] Lundh, J. S., Chatterjee, B., Dallas, J., Kim, H., and Choi, S., 2017, "Integrated Temperature Mapping of Lateral Gallium Nitride Electronics," *16th IEEE Intersociety Conference on Thermal and Thermomechanical Phenomena in Electronic Systems (ITherm)*, Orlando, FL, May 30–June 2, pp. 320–327.
- [48] Ju, Y. S., and Goodson, K. E., 1998, "Short-Time-Scale Thermal Mapping of Microdevices Using a Scanning Thermoreflectance Technique," *ASME J. Heat Transfer*, **120**(2), pp. 306–313.
- [49] Kendig, D., Tay, A. A. O., and Shakouri, A., 2016, "Thermal Imaging Based on Thermoreflectance Addresses the Challenges for Thermal Analysis of Today's Advanced Complex Devices," *17th International Conference on Electronic Packaging Technology (ICEPT)*, Wuhan, China, Aug. 16–19, pp. 1517–1521.
- [50] Long, D. A., 1977, *Raman Spectroscopy*, McGraw-Hill, New York, pp. 1–12.
- [51] Everall, N. J., 2009, "Confocal Raman Microscopy: Performance, Pitfalls, and Best Practice," *Appl. Spectrosc.*, **63**(9), pp. 245A–262A.
- [52] Dallas, J., Pavlidis, G., Chatterjee, B., Lundh, J. S., Ji, M., Kim, J., Kao, T., Detchprohm, T., Dupuis, R. D., Shen, S., Graham, S., and Choi, S., 2018, "Thermal Characterization of Gallium Nitride p-i-n Diodes," *Appl. Phys. Lett.*, **112**(7), p. 073503.
- [53] Heller, E. R., and Crespo, A., 2008, "Electro-Thermal Modeling of Multifinger AlGaIn/GaN HEMT Device Operation Including Thermal Substrate Effects," *Microelectron. Reliab.*, **48**(1), pp. 45–50.
- [54] Omura, I., Saito, W., Domon, T., and Tsuda, K., 2007, "Gallium Nitride Power HEMT for High Switching Frequency Power Electronics," *International Workshop on Physics of Semiconductor Devices*, Mumbai, India, Dec. 16–20, pp. 781–786.
- [55] Pavlidis, G., Kendig, D., Yates, L., and Graham, S., 2018, "Improving the Transient Thermal Characterization of GaN HEMTs," *17th IEEE Intersociety Conference on Thermal and Thermomechanical Phenomena in Electronic Systems (ITherm)*, San Diego, CA, May 29–June 1, pp. 208–213.
- [56] Baca, A. G., Armstrong, A. M., Allerman, A. A., Douglas, E. A., Sanchez, C. A., Michael, P., Coltrin, M. E., Fortune, T. R., Kaplar, R. J., Aln, A., Ga, A., Baca, A. G., Armstrong, A. M., Allerman, A. A., Douglas, E. A., Sanchez, C. A., King, M. P., Coltrin, M. E., Fortune, T. R., and Kaplar, R. J., 2016, "An AlN/Al<sub>0.85</sub>Ga<sub>0.15</sub>N High Electron Mobility Transistor," *Appl. Phys. Lett.*, **109**(3), p. 033509.
- [57] Baca, A. G., Klein, B. A., Allerman, A. A., Armstrong, A. M., Douglas, E. A., Stephenson, C. A., Fortune, T. R., and Kaplar, R. J., 2017, "Al<sub>0.85</sub>Ga<sub>0.15</sub>N/Al<sub>0.70</sub>Ga<sub>0.30</sub>N High Electron Mobility Transistors With Schottky Gates and Large On/Off Current Ratio Over Temperature," *ECS J. Solid State Sci. Technol.*, **6**(12), pp. Q161–Q165.
- [58] Baca, A. G., Armstrong, A. M., Allerman, A. A., Klein, B. A., Douglas, E. A., Sanchez, C. A., and Fortune, T. R., 2017, "High Temperature Operation of Al<sub>0.45</sub>Ga<sub>0.55</sub>N/Al<sub>0.30</sub>Ga<sub>0.70</sub>N High Electron Mobility Transistors," *ECS J. Solid State Sci. Technol.*, **6**(11), pp. S3010–S3013.
- [59] Chabak, K. D., Walker, D. E., Green, A. J., Crespo, A., Lindquist, M., Leedy, K., Tetlak, S., Gilbert, R., Moser, N. A., and Jessen, G., 2018, "Sub-Micron Gallium Oxide Radio Frequency Field-Effect Transistors," *IEEE MTT-S International Microwave Workshop Series on Advanced Materials and Processes for RF and THz Applications (IMWS-AMP)*, Ann Arbor, MI, July 16–18, pp. 1–3.
- [60] Green, A. J., Chabak, K. D., Baldini, M., Moser, N., Gilbert, R., Fitch, R. C., Wagner, G., Galazka, Z., McCandless, J., Crespo, A., Leedy, K., and Jessen, G. H., 2017, " $\beta$ -Ga<sub>2</sub>O<sub>3</sub> MOSFETs for Radio Frequency Operation," *IEEE Electron Device Lett.*, **38**(6), pp. 790–793.
- [61] Wong, M. H., Sasaki, K., Kuramata, A., Yamakoshi, S., and Higashiwaki, M., 2016, "Field-Plated Ga<sub>2</sub>O<sub>3</sub> MOSFETs With a Breakdown Voltage of Over 750V," *IEEE Electron Device Lett.*, **37**(2), pp. 212–215.
- [62] Koh, Y. K., and Cahill, D. G., 2007, "Frequency Dependence of the Thermal Conductivity of Semiconductor Alloys," *Phys. Rev. B Condens. Matter Mater. Phys.*, **76**(7), pp. 1–5.
- [63] Liu, W., and Balandin, A. A., 2005, "Thermal Conduction in Al<sub>x</sub>Ga<sub>1-x</sub>N Alloys and Thin Films," *J. Appl. Phys.*, **97**(7), p. 073710.